



UNIVERSITÀ
DEGLI STUDI
DI UDINE

Università degli studi di Udine

Piezoresistive Properties of Suspended Graphene Membranes under Uniaxial and Biaxial Strain in Nanoelectromechanical Pressure Sensors

Original

Availability:

This version is available <http://hdl.handle.net/11390/1100269> since 2021-03-23T12:24:01Z

Publisher:

Published

DOI:10.1021/acsnano.6b02533

Terms of use:

The institutional repository of the University of Udine (<http://air.uniud.it>) is provided by ARIC services. The aim is to enable open access to all the world.

Publisher copyright

(Article begins on next page)

Graphene-based Piezoresistive Sensors

Anderson D. Smith, Frank Niklaus, Alan Paussa, Sam Vaziri, Andreas C. Fischer, Mikael Sterner, Fredrik Forsberg, Anna Delin, David Esseni, Pierpaolo Palestri, Mikael Östling, Max C. Lemme*

Abstract

Graphene exhibits exceptional electronic and mechanical properties, making it a promising material for nanoelectromechanical (NEMS) devices. We conclusively demonstrate the piezoresistive effect in a graphene NEMS membrane that is highly relevant and generic for an important class of NEMS transducers. The graphene in our experiments acts as a strain gauge independent of crystallographic orientation with an average gauge factor of 2.9. The sensors have orders of magnitude higher sensitivity per unit area than conventional sensors.

* Corresponding author: max.lemme@uni-siegen.de

Graphene is an interesting material for nanoelectromechanical systems (NEMS) due to its high carrier mobility^{1,2}, a high Young's modulus of about 1 TPa³ and stretchability of up to approximately 20%.⁴ In addition, it shows strong adhesion to SiO₂ substrates⁵ and is nearly impermeable for gases, including helium.⁶ In this article, we demonstrate a piezoresistive pressure sensor based on a suspended graphene membrane with direct electrical signal read-out. We utilize a piezoresistive effect induced by mechanical strain in the graphene, which changes the electronic band structure⁷ and exploit the fact that the sensitivity of membrane-based electromechanical transducers strongly correlates with membrane thickness⁸. While graphene has been used as a piezoresistive strain gauge on silicon nitride⁹ and polymer membranes¹⁰, we use the graphene for both membrane and electromechanical transduction simultaneously with an average gauge factor of 2.92. The sensitivity per unit area of our graphene sensor is about 20 to 100s of times higher than conventional piezoresistive pressure sensors. The piezoresistive effect is nearly independent of crystallographic orientation.

In our experiments, graphene membranes made from chemical vapor deposited (CVD) graphene are suspended over cavities etched into a SiO₂ film on a silicon substrate. The graphene is electrically contacted and the devices are wire-bonded into a chip package. Process schematics are shown in Fig. 1a through c, while details of the fabrication process are described in the methods section. A scanning electron microscope image of a wire-bonded device and a photograph of a packaged device are shown in Fig. 1d and e respectively. If a pressure difference is present between the inside and the outside of the cavity (compare Fig. 1c), the graphene membrane that is

sealing the cavity is deflected and thus strained. This leads to a change of device resistivity due to the piezoresistive effect in the graphene.

Measurements were performed in an argon environment in order to reduce the effects of adsorbates. If air is used instead of argon for the experiments, adsorption of non-inert gases and/or molecules on the graphene will affect the resistivity.

In the experiments, the packaged device is placed inside a vacuum chamber. The chamber is then evacuated from atmospheric pressure down to 200 mbar, and then vented back to 1000 mbar. Thus the air sealed inside the cavity presses against the graphene membrane with a force proportional to the chamber pressure. The resistance of the graphene sensor is measured in a Wheatstone bridge (see supporting information), where the graphene membrane is one of the resistors in the bridge. The Wheatstone bridge is balanced at atmospheric pressure by adjusting a potentiometer to the same resistance value as the graphene membrane. The bridge is biased with 200mV square wave pulses with durations of 500 μ s. These values were chosen to avoid excessive heating of the graphene device. The voltage output signal from the Wheatstone bridge is amplified and low pass filtered before being sampled with an analog-to-digital converter and converted into its corresponding resistance value. The experimental conditions were chosen to remain within the expected tearing limits of the graphene membrane.⁵ The suspended membrane sensor is compared to a device with identical dimensions fabricated in parallel, but without a cavity. This is done in order to verify that it is indeed the presence of the cavity and the resulting mechanical bending and straining of the membrane that causes the pressure dependence

of the resistance. Fig. 2a shows the amplified voltage (with an amplification factor of 870) versus pressure curve for two devices, one with a cavity and one without. In contrast to the reference device without the cavity (blue hollow circles), the sensor device with the suspended graphene membrane (black squares) shows a strong correlation of the resistance with respect to pressure. This behavior is observed in several devices. Fig. 2a includes data of six measurement cycles, where each cycle represents one pump-down or one venting of the chamber. These measurements were performed in an argon environment in order to reduce the effects of adsorbates. Fig. 2b shows the same device held at constant pressures in order to see whether or not there is any drift present in the device. Note that, while there is a slight drift at several pressures, the resistance values show general consistency when held at fixed pressures.

Fig. 3a shows voltage versus pressure data for a non-cavity device tested in the most common gases found in air to assess the effect of adsorbates. As can be seen, there is a clear relationship of the resistance versus pressure of the air, which is less present when each gas is isolated. The offset in oxygen environment is due to not setting the resistance on the Wheatstone bridge between measurements. However, what is important to note is not the positions of the lines but their slopes. As one would expect, of all of the gasses tested, argon showed the least amount of reactivity with the devices. Argon was therefore used in the discussed experiments. Fig. 3b shows the average change in voltage of the cavity devices in comparison to the non-cavity devices. This data corresponds to two cavity devices and 3 non-cavity devices. As can be seen, there is a very strong correlation to the

device's sensitivity and the presence of a cavity. Fig. 3c shows a comparison of the change in voltage relative to a change in pressure for cavity devices and non-cavity devices for various cycling times. One cycle time corresponds to either one venting period or one pumping period. This experiment was done in order to eliminate the possibility of responses due to the Seebeck effect¹¹. If the Seebeck effect caused a significant change in the sensitivity, it would show also in the non-cavity cases. Since the non-cavity cases are stable, we conclude that the Seebeck effect is negligible.

Fig. 4a shows the same data as Fig. 2a split into separate pumping and venting cycles. Note that a slight hysteresis can be observed in those cycles that were run through a larger pressure range. Further, the graphene sensors have sensitivity only in a pressure range between roughly 1000 mbar and 500 mbar with the most drastic slopes occurring in the range of 600 to 900 mbar. Therefore, these pressure ranges were targeted. Fig. 4b shows resistance and pressure data as a function of time. This experiment served to reduce the pressure range to a level where the response was roughly linear. In fact, this measurement also explains the downward trend in Fig. 3c: the longer the cycle time the more saturation in the signal, and hence a smaller average change of voltage per pressure. Fig. 4c shows the change in voltage for two cavity and three non-cavity devices. Note that, regardless of the pump down speed, the change in voltage is generally consistent for both types (though one cavity device shows a higher change in voltage than the other). In contrast, all non-cavity devices showed a very weak response. This experiment confirms that the effect is due to straining of the graphene over

the cavity and not due to Seebeck heating and cooling as air is pumped and vented from the chamber. Fig. 4d is a comparison of the voltage change in the cavity and the non-cavity devices. These averages are taken from absolute values of the change in voltage so there is no accounting for how random noise will cause fluctuations in random directions. This is why the non-cavity cases give the appearance of being more sensitive in Fig. 4d than in Fig. 3b. The strong correlation between the presence of a cavity and the presence of the observed effect is strongly indicative of the piezoresistive effect, while simultaneously eliminating possible alternatives.

The sensitivity of piezoresistive membrane-based pressure sensors is given by Eq. 1, where S is the sensitivity, R is the resistance, V is the voltage, I is the current, and P is the pressure difference acting on the membrane.¹²

$$S = \frac{\Delta R}{R \cdot P} = \frac{\frac{\Delta V}{I}}{\frac{V}{I} \cdot P} = \frac{\Delta V}{V \cdot P} \quad (1)$$

If the current is held constant, then the sensitivity based on voltage measurements can be directly compared to the sensitivity based on the maximum change in resistance for a change in pressure of 477 mbar. The sensitivity of the piezoresistive graphene pressure sensor in Fig. 2 is measured to be 3.95 $\mu\text{V/V/mmHg}$. Table 2 in the supporting information compares the sensitivity of our sensor with conventional piezoresistive Si-based and carbon nanotube (CNT) based pressure sensors reported in literature.²⁰⁻²³ The graphene membrane-based pressure sensor, though much smaller than conventional piezoresistive pressure sensors, outperforms all the listed sensors in sensitivity, with the exception of the one with by far the largest dimensions.

In general, the sensitivity S of membrane-based piezoresistive pressure sensors is dependent on the membrane material characteristics, the membrane thickness and the membrane area.¹² Eq. 2 describes the respective relations, where P is the pressure, ν is Poisson's ratio of the membrane material, E is the Young's modulus of the membrane material, a^2 is the membrane area, and h is the membrane thickness.

$$S \propto \frac{P(1-\nu^2)}{E} \left(\frac{a}{h}\right)^2 \quad (2)$$

Thus, the sensitivity of piezoresistive pressure sensors with different membrane areas can be directly compared by normalizing the sensitivity to a standard membrane area. When normalizing the sensitivity of the pressure sensors from Table 2 of the supporting information to a standard membrane area, the sensitivity of our graphene sensor is about 20 to 100s of times higher than the other sensors (Fig. 5). This and the fact that the graphene sensor is already smaller in area than any of the other sensors indicate great potential for further size-reduction of graphene membrane-based sensors.

In order to estimate the piezoresistive gauge factor of the graphene transducer in our sensor, the change in resistance of the cavity region must be determined. A finite element analysis of the deflection was performed using COMSOL multiphysics and calibrated using literature data of graphene membrane deflection obtained by atomic force microscopy.⁵ The model consists of linearly elastic 2D thin plate elements with isotropic stiffness clamped along the boundary of the cavity and actuated by a homogenous differential pressure load over the whole surface. Geometric nonlinearity was considered in the analysis, and for numerical stability the pressure was

ramped from 0 to the nominal value. The strain for the gauge factor was evaluated by averaging the uniaxial strain in the main current direction over the whole membrane, in the direction of the short axis of the cavity. Material parameters taken from literature were used in the COMSOL model such as the elastic constant $Et = 347 \text{ N/m}$, where E is the Young's modulus, t is the membrane thickness ($t = 0.335 \text{ nm}$) and Poisson's ratio $\nu = 0.16$. A compilation of the comparison between the model and measured literature values is shown in Table 2 of the supporting information. Good agreement is noted both with the measurements of a $2.3 \mu\text{m}$ radius circular membrane in Koenig et al.⁵ and with the measurement in Bunch *et al.* on a square $4.75 \mu\text{m} \times 4.75 \mu\text{m}$ membrane at a pressure difference of 930 mbar.⁶ The derived model was then applied to the $6 \mu\text{m}$ by $64 \mu\text{m}$ cavity used in the current experiment to estimate the deflection of the membrane. At a pressure difference of 477 mbar, the deflection of the membrane is calculated to be 202 nm (Fig. 6a), which results in an average strain of 0.29 % across the membrane.

An electrically equivalent circuit of the sensor is schematically shown in Fig. 6b and is described in Eq. 3

$$R_{tot} = R_1 + \frac{1}{\frac{1}{R_2} + \frac{1}{R_4} + \frac{1}{R_5}} + R_3 \quad (3)$$

The total resistance R_{tot} is taken from resistance measurements at chamber pressures of 1000 mbar and 523 mbar (Fig. 2a). The resistances R_1 through R_5 correspond to the resistances of the regions shown in Figure 6b. R_2 represents the resistance of the graphene membrane over the cavity and we assume that only R_2 changes as a function of pressure. The resistance R

for each region in Fig. 6b can be described by Eq. 4, where L is the length between the contacts, A is the cross-sectional area, and ρ is the resistivity.

$$R = \rho \frac{L}{A} \quad (4)$$

Assuming as a first order approximation that the graphene resistivity at ambient pressure is identical over the cavity and next to the cavity, one can extract individual resistances for each component of the total resistance for the case of 1000 mbar. Then, the change in resistance is approximately 1 Ω at a pressure difference of $P = 477$ mbar. Using this method, R_2 is determined to be 0.191 k Ω at 1000 mbar, and the percent resistance change of the graphene membrane patch (R_2) is determined to be 0.59%.

The gauge factor in our sensor was then calculated as the percent change in resistance divided by the percent change in strain to be 3.67. Gauge factors vary depending on the pressure range measured with a maximum value of 4.33 and an average value of 2.92. As can be seen in Fig. 2a, there is a saturation of the resistance change below a certain chamber pressure. This effect is most likely explained by delamination of the graphene at the edge of the cavity. Previous literature, by comparison, reports gauge factors of 1.9 for suspended graphene beams¹³, about 150 for graphene on SiO₂¹⁴ and nearly 18000 for graphene on a silicon nitride membrane.⁹

Simulations of the change of the graphene pressure sensor resistance due to strain were carried out in order to interpret the experimental results. For a low electric field in the transport direction and considering a Fermi level close to the Dirac energy ($E_F = 0$ eV), the resistance R_2 of the graphene foil suspended over the cavity is expressed as

$$R_2 = \rho \frac{L'}{W_t'} = \frac{1}{2qN_e\mu_e} \frac{(1 + \varepsilon_{xx})L}{(1 + \varepsilon_{yy})W_t'}, \quad (5)$$

where ρ is the resistivity of the suspended graphene sheet, N_e and μ_e are respectively the electron density and the corresponding mobility (that are assumed to be the same as the hole density and hole mobility, respectively, since we set $E_F=0\text{eV}$), ε_{xx} and ε_{yy} are the components of the strain tensor respectively in the direction of the transport and normal to the transport, and q is the positive electron charge. Note that the strain induced in graphene by the pressure difference between the cavity and the chamber Δp influences both the terms L' and W_t' related to the geometry as well as the resistivity ρ .

The induced strain can be considered quasi-uniaxial since its component in the direction of the transport is dominant ($\varepsilon_{xx} \gg \varepsilon_{yy}$). If ρ is not modified by strain, the change of L and W_t alone is not enough to explain the experimental resistance change with strain.

Then, the influence of strain on ρ has been analyzed by starting with the effect of strain on the electron density N_e , simulated by employing the strained graphene bandstructure stemming from the Tight-Binding (TB) Hamiltonian presented in Pereira et. al⁷. N_e increases with the strain, which, in contrast with the experiments (see Fig. 2a), would lead to a decrease of the resistivity (see Eq.5 and supporting information). Hence the changes in the graphene charge are not sufficient to explain the observed change of the resistance R_2 with the strain. The effect of capacitive coupling was also explored through simulation and, though present, is found to cause changes in resistance much lower than those observed experimentally.

For this reason the effect of the strain on the mobility μ_e is simulated by solving the Linearized Boltzmann Transport Equation (LBTE)²⁴. This approach gives the exact solution of the LBTE even in the presence of anisotropic and non-monotonic energy dispersion relation and anisotropic scattering rates. In these calculations Neutral Defects (ND)²⁵ are considered, which are dominant in CVD graphene²⁶. The electron mobility decreases with increasing Δp (see supporting information). Such mobility degradation more than compensates the N_e enhancement, so that the calculations lead to an overall R_2 increase. Fig. 6c compares the simulated versus measured R_2 modulation versus Δp . As can be seen the simulation results do not critically depend on whether the strain is uniaxial or biaxial and the overall agreement with experiments is reasonably good. Fig. 6d compares the corresponding calculated and measured gauge factors; the biaxial or uniaxial nature of the strain has a modest influence on the gauge factor. Simulation data from Huang et al. are also included for reference.¹³ Note also that, due to the flexibility of the approach, the relative variation of R_2 is independent of the graphene orientation with respect to the direction of the transport (Fig. 6e and 6f), of the defect concentration, and of the considered Fermi level (i.e. the carrier density). This is an important aspect of our work, because it makes the approach independent of random crystallographic alignment and multiple grain graphene flakes.

The piezoresistive effect in graphene was demonstrated in a graphene–membrane pressure sensor. The sensitivity of piezoresistive graphene sensors is superior to silicon and CNT-based sensors and orders of

magnitude more sensitive when normalized for membrane dimensions. This is in line with theoretical considerations that indicate such a decisive advantage due to graphene's extraordinary thinness. A finite element simulation is derived to describe the deflection of graphene membranes over sealed cavities as a function of pressure and verified with literature data. The estimated maximum gauge factor for graphene based on this model is 4.33 with values averaging at 2.92. Tight binding calculations support the experimental data, including only a small dependence of the observed effect on crystal orientation. This work demonstrates that thin graphene membranes can be efficiently implemented as piezoresistive transducer elements for emerging NEMS sensors.

Methods

Devices are fabricated on p-type silicon substrates with a thermally grown silicon dioxide (SiO_2) layer of $1.5\ \mu\text{m}$. Rectangular cavities of $6\ \mu\text{m}$ by $64\ \mu\text{m}$ are etched $650\ \text{nm}$ deep into the SiO_2 using a resist mask and an Ar and CHF_3 -based reactive ion etching (RIE) process at 200mW and $40\ \text{mTorr}$ to provide vertical etch profiles. Next, contact areas are defined by lithography and etched $640\ \text{nm}$ into the SiO_2 layer using again an RIE process. The contact cavities are then filled with a $160\ \text{nm}$ layer of titanium followed by a $500\ \text{nm}$ layer of gold using metal evaporation so that the contacts are raised about $20\ \text{nm}$ above the surface of the SiO_2 . The contacts are buried to prevent wire bonding from ripping the contacts off of the substrate. This has the added advantage of allowing the graphene to be transferred in a later step, which improves the cleanliness of the process and reduces the risk of rupturing the graphene membranes during processing. Also, the graphene-metal contacts are not degraded by polymer residues in this way.

Commercially available chemical vapor deposited (CVD) monolayer graphene films on copper foils are used. The graphene on one side of the copper is spin-coated with either a poly(methyl methacrylate) (PMMA) or poly(Bisphenol A) carbonate (PC) layer in order to act as a mediator between the initial and final substrate¹⁵⁻¹⁹. The graphene on the backside of the foil is etched using O_2 plasma and the copper foil is subsequently wet etched in FeCl_3 and then transferred into de-ionized water. The bottom left of Fig. 2a shows a contrast enhanced image of graphene with a polymer coating floating in a solution of FeCl_3 after the copper is etched away. The PMMA/graphene film is picked up with the chip and dried on a hotplate. After drying, the chip is placed into a

solution of Chloroform overnight in order to etch the PC polymer layer. Next, a photoresist layer is applied and exposed in order to pattern the graphene. Finally, the graphene is etched into the desired shape using an O₂ plasma etch and the photoresist is removed in acetone. Once the devices are fabricated, the chips are placed into a chip housing and gold wires are bonded from the housing to the contact pads. The layout of the contacts is shown schematically in Fig. 1c and the wire bonded device is shown in a scanning electron micrograph in Fig. 1d, Raman spectroscopy and electrical measurements were performed to verify the presence of graphene (see supporting information).

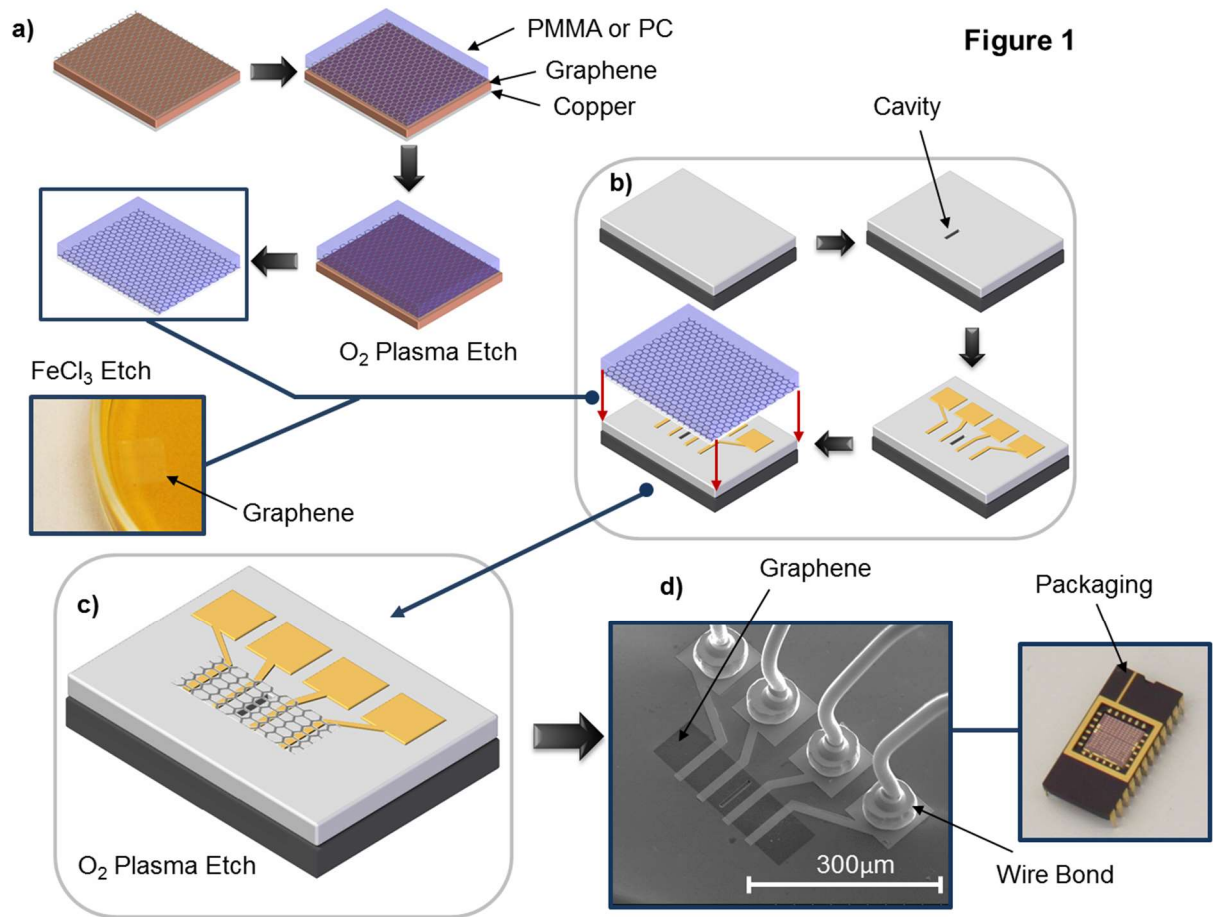


Figure 1: a) A Layer of PMMA or PC is applied to one side of chemical vapor deposited (CVD) graphene on copper foil. Graphene is then etched from the back side of the copper foil using O_2 plasma. Finally, the copper is etched using $FeCl_3$. b) Fabrication sequence of the pressure sensor and the corresponding transfer of graphene onto the substrate. Once the graphene is transferred to the chip, the polymer layer is removed and the graphene is etched (c)). After fabrication of the devices, they are packaged and wire bonded (d).

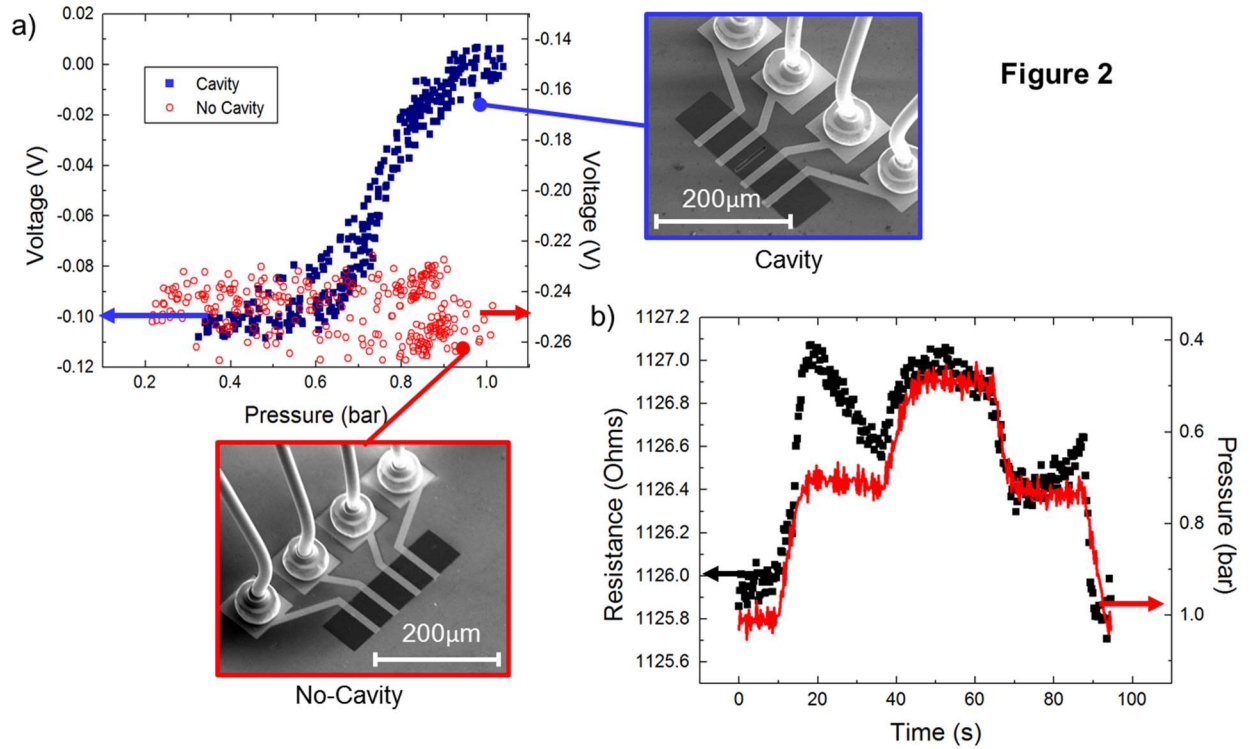


Figure 2: a) Pressure versus voltage measurements of a device with a cavity (blue squares) and a device without a cavity (red hollow circles). There is a clear dependence in the case of the device with a cavity, where the pressure difference leads to bending and strain in the graphene membrane. This dependence is not observed in the unsuspended device. b) Resistance of the same cavity device (black squares) compared to the pressure (red line). The pressure was held constant at different levels.

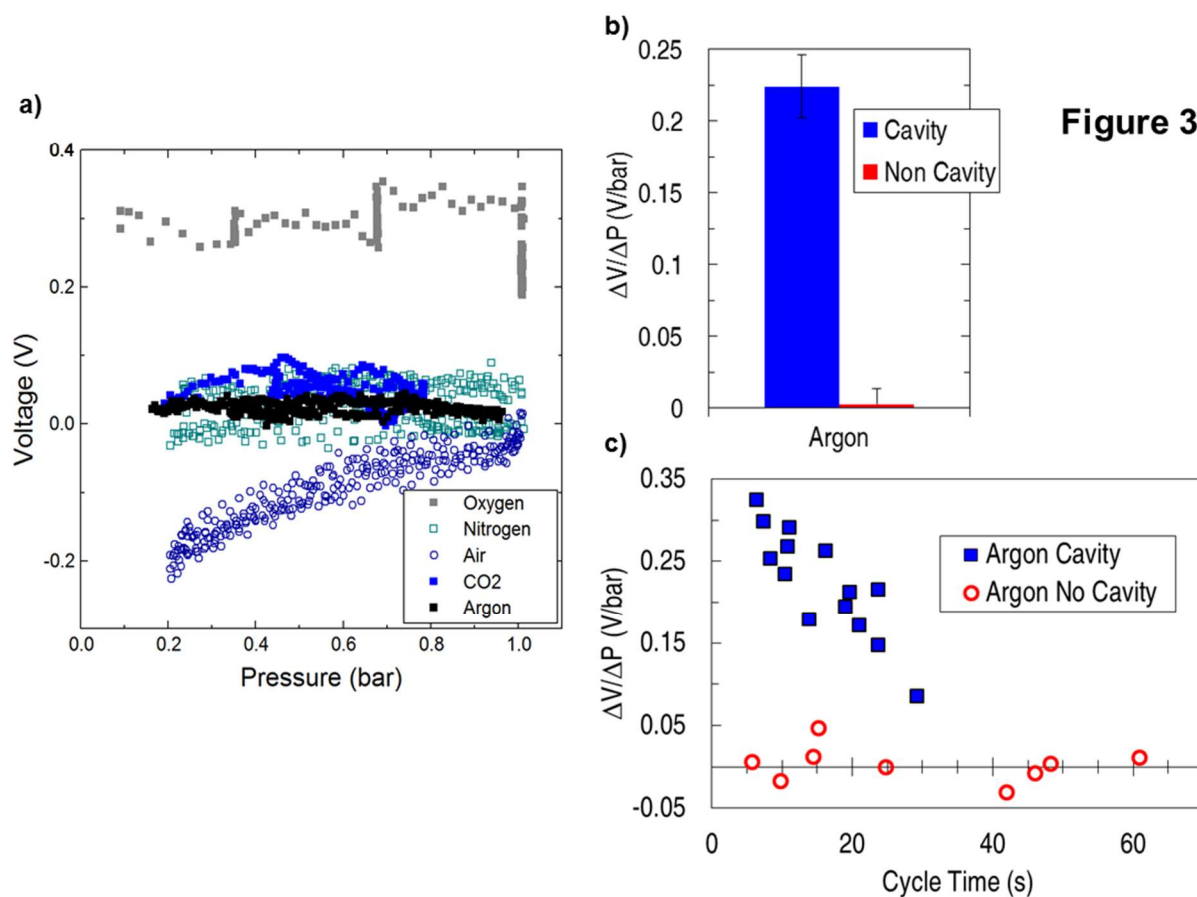


Figure 3: a) Voltage versus pressure characteristics for a non-cavity device which was measured in oxygen, CO₂, nitrogen, argon, and air in order to assess the effect of adsorbates on the devices. b) Average rate of change of the voltage relative to the pressure for the cavity devices compared to the non-cavity devices. Error bars show their respective standard deviation. c) Comparison of the rate of change in voltage versus pressure ($\Delta V/\Delta P$) for several cavity and non-cavity devices measured in Argon for different cycle times for both pumping and venting.

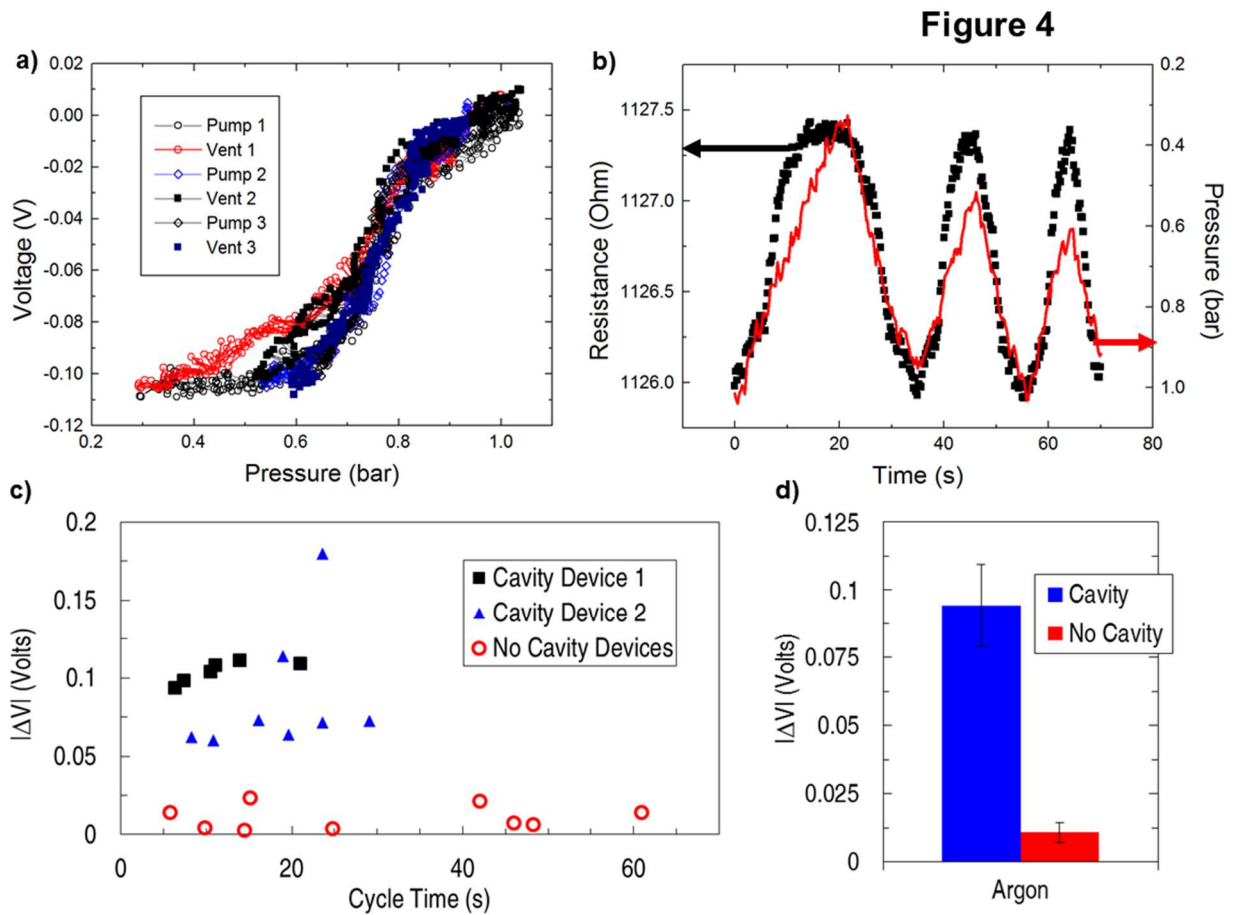


Figure 4: a) Different pump and vent cycles for a cavity device. b), Voltage dependence of the device compared to the pressure measured on the reference pressure gauge for different cycles in order to assess the sensitivity range of the device. They are most sensitive from 1 bar to approximately 0.5 bar. c), Changes in voltage compared for both cavity and non-cavity devices, showing stable devices operation for different pump and vent cycle speeds. d) Comparison of the absolute value of the average changes in voltage of both the cavity and non-cavity cases. The error bars represent the standard deviations of the devices.

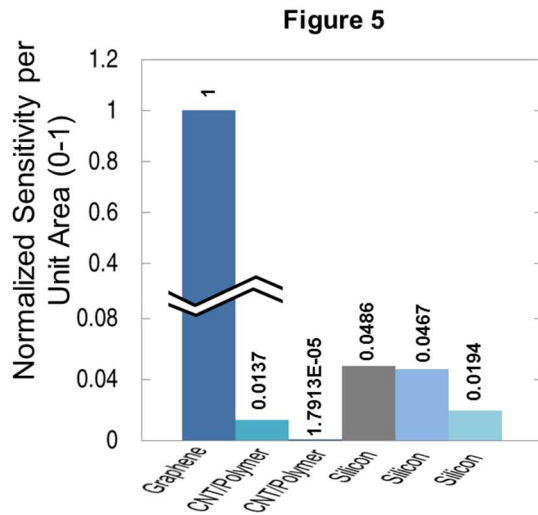


Figure 5: Normalized sensitivity per unit area for the graphene pressure sensors in this paper compared to silicon and carbon nanotube-based sensors.²⁰⁻²³ The graphene sensor is roughly 20 to 100 times more sensitive per unit area than the conventional MEMS sensors showing the potential for aggressive scaling. Tabulated sensitivity values are shown in the supporting information.²⁰⁻²³

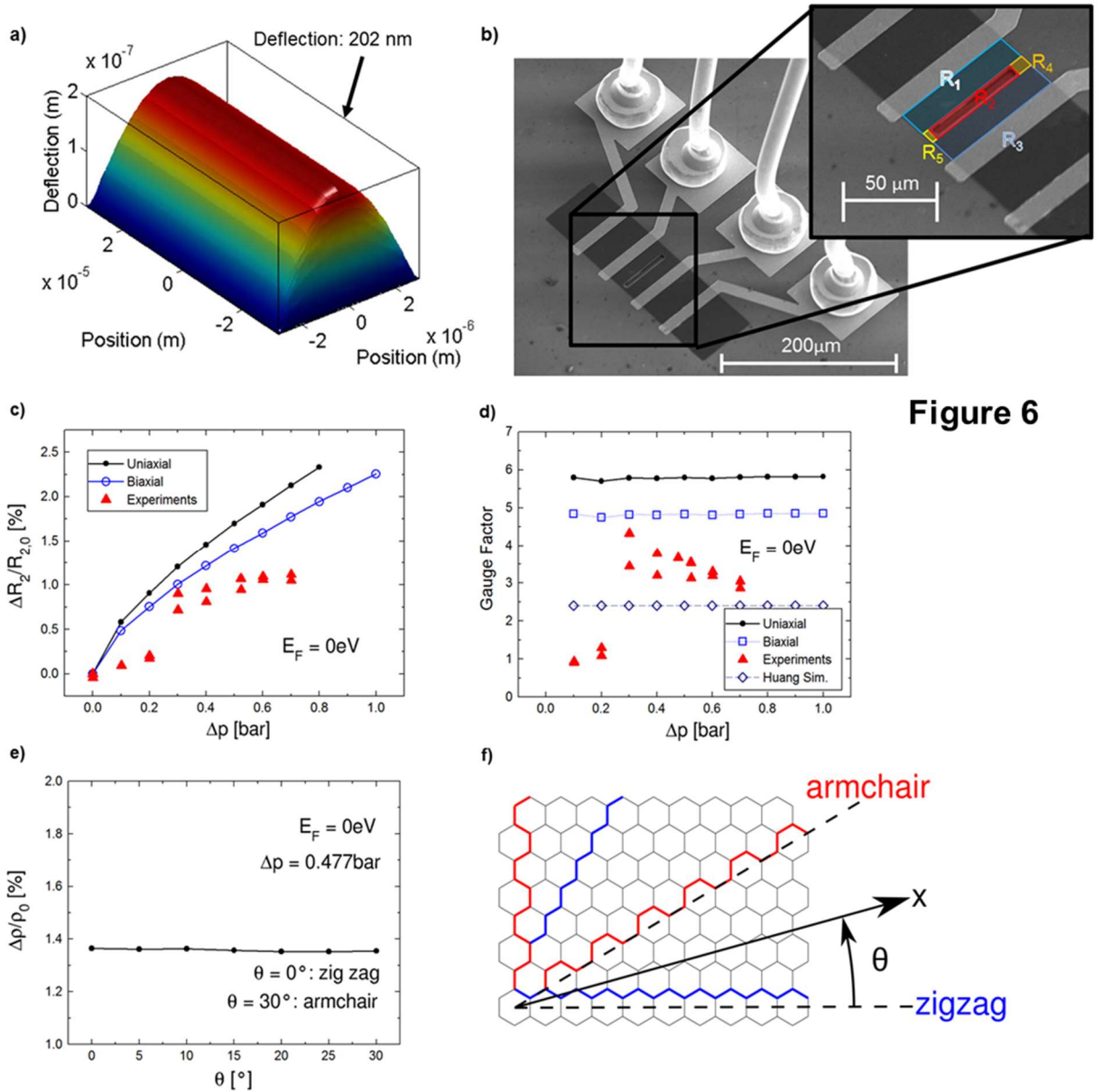


Figure 6: a) Model of the cavity deflection for the membrane dimensions in the experiment. The plot shows one half of the symmetric 6 μm by 64 μm membrane in the deflected state at a pressure difference of 477 mbar giving a total deflection of 202 nm. b) Different components of the resistor model that was used in order to calculate a gauge factor based on the experimental results. Simulated (lines) and experimental (triangles) relative variation of R_2 (c) and the relative gauge factor (6d) versus Δp . Simulation results by Huang et al. added for reference.¹³ e)

Schematic of the definition of the crystallographic angles used for the calculations in this work. f) Simulation showing that the strain effect on resistivity is independent of the strain angle.

References

1. Bolotin, K. I.; Sikes, K.; Jiang, Z.; Klima, M.; Fudenberg, G.; Hone, J.; Kim, P.; Stormer, H., Ultrahigh electron mobility in suspended graphene. *Solid State Communications* **2008**, *146* (9), 351-355.
2. Morozov, S.; Novoselov, K.; Katsnelson, M.; Schedin, F.; Elias, D.; Jaszczak, J.; Geim, A., Giant intrinsic carrier mobilities in graphene and its bilayer. *Physical Review Letters* **2008**, *100* (1), 16602.
3. Lee, C.; Wei, X.; Kysar, J. W.; Hone, J., Measurement of the elastic properties and intrinsic strength of monolayer graphene. *Science* **2008**, *321* (5887), 385-388.
4. Tomori, H.; Kanda, A.; Goto, H.; Ootuka, Y.; Tsukagoshi, K.; Moriyama, S.; Watanabe, E.; Tsuya, D., Introducing Nonuniform Strain to Graphene Using Dielectric Nanopillars. *Appl. Phys. Express* **2011**, *4*, 075102.
5. Koenig, S. P.; Boddeti, N. G.; Dunn, M. L.; Bunch, J. S., Ultrastrong adhesion of graphene membranes. *Nature nanotechnology* **2011**, *6* (9), 543-546.
6. Bunch, J. S.; Verbridge, S. S.; Alden, J. S.; Van Der Zande, A. M.; Parpia, J. M.; Craighead, H. G.; McEuen, P. L., Impermeable atomic membranes from graphene sheets. *Nano letters* **2008**, *8* (8), 2458-2462.
7. Pereira, V. M.; Neto, A. C.; Peres, N., Tight-binding approach to uniaxial strain in graphene. *Physical Review* **2009**, *80* (4), 045401.
8. Gong, S.-C.; Lee, C., Analytical solutions of sensitivity for pressure microsensors. *Sensors Journal, IEEE* **2001**, *1* (4), 340-344.
9. Hosseinzadegan, H.; Todd, C.; Lal, A.; Pandey, M.; Levendorf, M.; Park, J. In *Graphene has ultra high piezoresistive gauge factor*, Micro Electro Mechanical Systems (MEMS), IEEE 25th International Conference **2012**, 611-614.
10. Kim, K. S.; Zhao, Y.; Jang, H.; Lee, S. Y.; Kim, J. M.; Kim, K. S.; Ahn, J.-H.; Kim, P.; Choi, J.-Y.; Hong, B. H., Large-scale pattern growth of graphene films for stretchable transparent electrodes. *Nature* **2009**, *457* (7230), 706-710.
11. Li, X.; Yin, J.; Zhou, J.; Wang, Q.; Guo, W., Exceptional high Seebeck coefficient and gas-flow-induced voltage in multilayer graphene. *Applied Physics Letters* **2012**, *100* (18), 183108-183108-4.
12. Melvås, P. Ultraminiaturized Pressure Sensor for Catheter Based Applications. Ph.D. thesis, KTH Royal Institute of Technology, **2002**.
13. Huang, M.; Pascal, T. A.; Kim, H.; Goddard III, W. A.; Greer, J. R., Electronic-mechanical coupling in graphene from in situ nanoindentation experiments and multiscale atomistic simulations. *Nano letters* **2011**, *11* (3), 1241-1246.
14. Chen, X.; Zheng, X.; Kim, J.-K.; Li, X.; Lee, D.-W., Investigation of graphene piezoresistors for use as strain gauge sensors. *Journal of Vacuum Science & Technology B: Microelectronics and Nanometer Structures* **2011**, *29* (6), 06FE01-06FE01-5.
15. Reina, A.; Son, H.; Jiao, L.; Fan, B.; Dresselhaus, M. S.; Liu, Z.; Kong, J., Transferring and identification of single-and few-layer graphene on arbitrary substrates. *The Journal of Physical Chemistry C* **2008**, *112* (46), 17741-17744.
16. Li, X.; Zhu, Y.; Cai, W.; Borysiak, M.; Han, B.; Chen, D.; Piner, R. D.; Colombo, L.; Ruoff, R. S., Transfer of large-area graphene films for high-performance transparent conductive electrodes. *Nano letters* **2009**, *9* (12), 4359-4363.
17. Jiao, L.; Fan, B.; Xian, X.; Wu, Z.; Zhang, J.; Liu, Z., Creation of nanostructures with poly (methyl methacrylate)-mediated nanotransfer printing. *Journal of the American Chemical Society* **2008**, *130* (38), 12612-12613.
18. Park, H. J.; Meyer, J.; Roth, S.; Skákalová, V., Growth and properties of few-layer graphene prepared by chemical vapor deposition. *Carbon* **2010**, *48* (4), 1088-1094.

19. Lin, Y.-C.; Jin, C.; Lee, J.-C.; Jen, S.-F.; Suenaga, K.; Chiu, P.-W., Clean transfer of graphene for isolation and suspension. *ACS Nano* **2011**, 2362-2368.
20. Hierold, C.; Jungen, A.; Stampfer, C.; Helbling, T., Nano electromechanical sensors based on carbon nanotubes. *Sensors and Actuators A: Physical* **2007**, 136 (1), 51-61.
21. Fung, C. K.; Zhang, M. Q.; Chan, R. H.; Li, W. J. In *A PMMA-based micro pressure sensor chip using carbon nanotubes as sensing elements*, *Micro Electro Mechanical Systems* **2005**. MEMS 18th IEEE International Conference, 251-254.
22. Christel, L.; Petersen, K. In *A catheter pressure sensor with side vent using multiple silicon fusion bonding*, *Proc. Int. Conf. Solid-State Sensors and Actuators (Transducers)* **1993**; 620-623.
23. Kalvesten, E.; Smith, L.; Tenerz, L.; Stemme, G. The first surface micromachined pressure sensor for cardiovascular pressure measurements, *Micro Electro Mechanical Systems* **1998**. MEMS 98. Proceedings., The Eleventh Annual International Workshop, 574-579.
24. Paussa, A.; Esseni, D., An exact solution of the linearized Boltzmann transport equation and its application to mobility calculations in graphene bilayers. *Journal of Applied Physics* **2013**, 113, 093702.
25. Bresciani, M.; Paussa, A.; Palestri, P.; Esseni, D.; Selmi, L. Low-field mobility and high-field drift velocity in graphene nanoribbons and graphene bilayers, *Electron Devices Meeting (IEDM), 2010 IEEE International* **2010**, 32.1. 1-32.1. 4.
26. Iyechika, Y., Application of Graphene to High-Speed Transistors: Expectations and Challenges. *Science and technology trends* **2010**, 37, 76-92.